



## Fracture toughness of exponential layer-by-layer polyurethane/poly(acrylic acid) nanocomposite films

E. Kheng<sup>a</sup>, H.R. Iyer<sup>a</sup>, P. Podsiadlo<sup>c,d</sup>, A.K. Kaushik<sup>a</sup>, N.A. Kotov<sup>c</sup>, E.M. Arruda<sup>a</sup>, A.M. Waas<sup>a,b,\*</sup>

<sup>a</sup> Department of Mechanical Engineering, University of Michigan, Ann Arbor, MI 48109, USA

<sup>b</sup> Department of Aerospace Engineering, University of Michigan, Ann Arbor, MI 48109, USA

<sup>c</sup> Department of Chemical Engineering, University of Michigan, Ann Arbor, MI 48109, USA

<sup>d</sup> Center for Nanoscale Materials, Argonne National Laboratory, Argonne, IL 60439, USA

### ARTICLE INFO

#### Article history:

Received 29 January 2010

Received in revised form 27 July 2010

Accepted 8 August 2010

Available online 31 August 2010

#### Keywords:

Nanocomposite

Fracture toughness

Thin film

Finite strain

Finite elements

### ABSTRACT

This paper characterizes the fracture toughness of layer-by-layer (LBL) manufactured thin films with elastic polyurethane, a tough polymer, and poly(acrylic acid) as a stiffening agent. A single-edge-notch tension (SENT) specimen is used to study mode I crack propagation as a function of applied loading. Experimental results for the full-field time histories of the strain maps in the fracturing film have been analyzed to obtain *R*-curve parameters for the nanocomposite. In particular, by using the strain maps, details of the traction law are measured. A validated finite strain phenomenological visco-plastic constitutive model is used to characterize the nanocomposite film while a discrete cohesive zone model (DCZM) is implemented to model the fracture behavior. The LBL manufactured nanocomposite is found to display a higher fracture toughness than the unstiffened base polymer.

© 2010 Elsevier Ltd. All rights reserved.

## 1. Introduction

There is growing interest in manufacturing synthetic nanocomposites with nano-scale control, that have the fine hierarchical structure found in natural nanocomposites, such as seashell nacre, bone, or spider silk [1–3]. Such nanocomposites are found to display exceptional mechanical properties, e.g. fracture toughness, strength and stiffness, often exceeding the properties of man made synthetics. The layer-by-layer (LBL) manufacturing technique [4] has been used to produce hierarchically structured materials with very high strengths and stiffnesses relative to their constituent materials [5–7]. A necessary drawback of LBL manufacturing is the slow deposition rate, which limits the shape and form of materials prepared with this method to thin films and coatings.

Of concern in this paper is the characterization of fracture toughness of exponential LBL manufactured polymer nanocomposites composed of a water-soluble polymer and a water-soluble stiffening agent that has a good distribution of the hardening agent through the polymer matrix [6,7]. The exponential LBL method has lead to a significant reduction in the manufacturing time of the assembled films. The polymer and the stiffening agent are oppositely charged, resulting in strong ionic bonds between the polymer matrix and the hardening agent. In the present study, tough and elastic polyurethane is used as the base matrix polymer, and poly(acrylic acid) is used as the stiffening agent, resulting in a nanocomposite with improved stiffness and considerable ductility.

When a pre-existing crack in these films is advanced by the application of mechanical loads, severe crack blunting is first observed with a large plastic zone surrounding the crack tip that dissipates energy. This plastic zone can activate several nano-scale mechanisms that leads to a *R*-curve response [8]. The additional toughening is regarded as a basic material

\* Corresponding author at: Department of Mechanical Engineering, University of Michigan, Ann Arbor, MI 48109, USA.

E-mail address: [dcw@umich.edu](mailto:dcw@umich.edu) (A.M. Waas).

property that can be captured by a homogenized, non-linear traction-separation law, in conjunction with a suitable finite element simulation of specimen geometry and loading. In order to carry out this analysis, it is also necessary to characterize the constitutive response of the films undergoing finite deformation.

The fracture toughness is measured by carrying out a series of single edge-notch tension mode-I fracture tests on free standing nanocomposite thin films (plane stress). Numerical simulation of the fracture tests in association with an accurate finite deformation constitutive model for the film material leads to a method that allows calculation of the fracture energy. In the numerical simulation, carried out using the commercial software ABAQUS, a discrete cohesive zone model (DCZM) [10] is implemented to represent the material ahead of the initial crack. During the quasi-static growth of the crack, an increment of external work input is balanced by the sum of the stored strain energy, the plastic energy dissipated and the energy associated with fracture. Therefore the latter can be determined by knowing the plastic energy dissipated, the elastic energy stored and the external work done to advance the crack.

To accurately obtain the plastic energy dissipated while accounting for loading rate effects, the film's constitutive behavior has to be accurately modeled for both loading and unloading that occurs during the crack growth event. A phenomenological visco-plastic constitutive model, which is an extension of the Arruda–Boyce model [15,13], is used to capture the non-linear large strain visco-plastic behavior with large residual plastic strains after unloading.

The DCZM elements which represent the fracture zone are prescribed through a non-linear traction-separation law which is iterated to match the numerical predictions to the experimental measurements. A traction-separation law has two defining characteristics – the cohesive strength and the fracture toughness [18]. Since the cohesive strength can be determined from careful examination of the experimental strains, the fracture toughness distribution is the only unknown for which iteration is needed. The traction-separation law numerically reproducing the experiment therefore provides the fracture toughness distribution in the fracture zone. The fracture toughness distribution that results in the best match of the numerical simulation to the experiment gives us insight to the toughening mechanisms at work in the fracture zone. *R*-curve behavior is observed along the fracture zone. A larger fracture toughness and cohesive strength are observed further from the initial crack, implying that both these quantities are increased as more plastic work is done in the neighboring substrate as the crack advances.

## 2. Experiments

### 2.1. Manufacturing the films and samples

The films are manufactured by alternately dipping glass slides into dilute aqueous dispersions (1 wt.%) of positively charged polyurethane and negatively charged poly(acrylic acid) (PU/PAA). To manufacture a single film, this process is repeated 100 times and produces a thin film that has an average thickness of 40  $\mu\text{m}$ . The films are detached from the glass slide using hydro-fluoric acid and then dried in a heated chamber. Single-film samples are manufactured on standard microscope glass slides, resulting in a length of approximately 70 mm and a height of 25 mm. These are cut to the appropriate sizes for various characterization tests. A free standing film is shown in Fig. 1. The PU/PAA samples discussed in this paper are all five-film stacks, and are manufactured by pressing five single-film samples together in a heated hydraulic press at 110  $^{\circ}\text{C}$  and 15 MPa for 30 min. A pure cationic polyurethane (PU) sample is also made from the polyurethane solution by heating the solution in a petri dish, thereby removing the water molecules. The pure PU sample is studied for the purpose of comparison.

### 2.2. Tensile tests of the films

The strain rate-dependent properties of the films are measured by tensile tests using specimens illustrated in Fig. 2. Tensile test samples are manufactured to a total length of  $25 \pm 1$  mm, a gauge length of  $13 \pm 2$  mm and a height of  $2.5 \pm 0.5$  mm.



Fig. 1. Photograph of translucent eLBL PU/PAA film after detaching and heating.

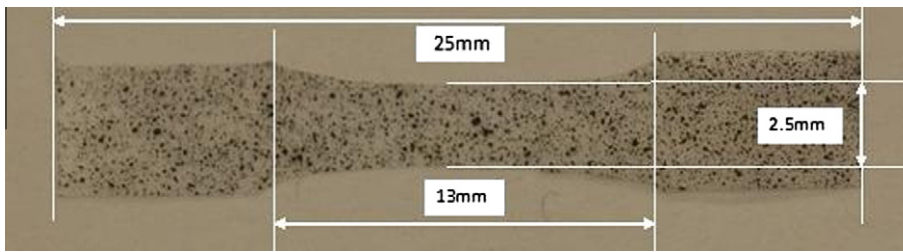


Fig. 2. Tensile test specimens.

The tests were carried out on samples that were between 200  $\mu\text{m}$  and 300  $\mu\text{m}$  thick, under displacement control loading at nominal rates of 0.16 mm/s and 0.016 mm/s. Characteristic engineering stress–engineering strain curves for the samples are shown in Fig. 3. Strains are determined using optical images taken with a high resolution camera of a speckle pattern distributed on the surface of the film using acrylic paint applied with an airbrush, and the tensile force in the specimens is measured with a load cell attached to the mechanical testing machine. Thicknesses of the samples are measured with the aid of a scanning electron microscope. The samples are coated with a 5 nm thick gold layer to prevent charging and damage of the sample in the scanning electron microscope. The tensile test results are used to characterize the film material for the finite element model that is used in the present work.

### 2.3. Single notch fracture tests

The fracture toughness of a thin film in plane stress is measured by matching numerical simulations to physical experiments of a single-edge-notch tension mode-I fracture test. This section describes these experimental fracture tests.

The samples are attached to flat sample holders with a thin layer of epoxy and a single notch is made with a surgical razor blade in the film perpendicular to an edge as shown in Fig. 4. The free standing film between the sample holders is  $5 \pm 0.3$  mm by  $25 \pm 2$  mm. The initial crack is cut to dimension of  $4.5 \pm 0.5$  mm, leaving an un-fractured height,  $h_0$ , of  $20.5 \pm 0.5$  mm. A fixed coordinate system is used to discuss the experimental results and associated numerical simulation results. The origin of the coordinate system is located along the expected crack plane, at the midpoint of the height of the specimen, as indicated in Fig. 4. The fracture tests are carried out on a displacement controlled table-top tensile test setup with a step-motor drive. The setup is shown in Fig. 5. The displacement rate is set to 0.003 mm/s. Images of the speckle pattern are captured once every ten seconds. The displacement between the sample holders is measured with a linear variable differential transformer (LVDT) and is confirmed with the data obtained from the speckle pattern. The tensile forces are measured with a 150 N load cell. The resolution of the load cell is 0.0068 N, which corresponds to a resolution in stress of 0.0013 MPa. The resolution of the LVDT is 0.00012 mm. The strain resolution of the digital image correlation technique is 0.001.

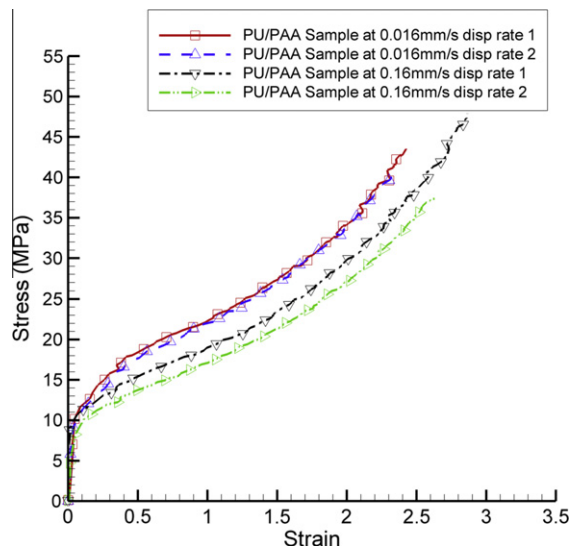


Fig. 3. Characteristic engineering stress–engineering strain curves of 5 film PU/PAA stacks at different stretch rates.

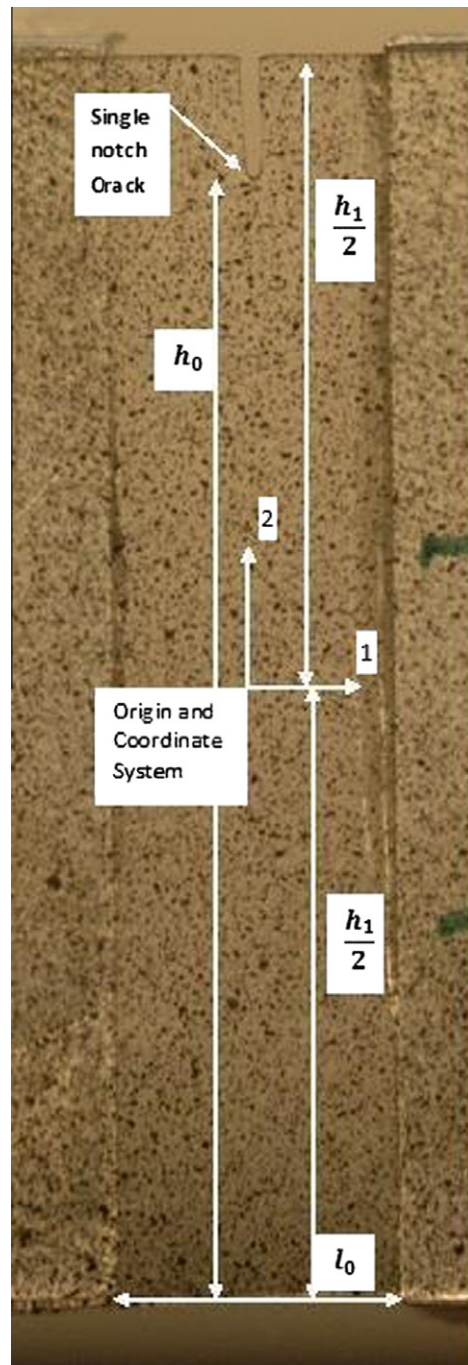


Fig. 4. Dimensions of experimental setup of film samples.

#### 2.4. Force displacement description of fracture tests

The PU/PAA samples all fractured in a uniform manner, with the crack propagating cleanly through the un-fractured height of the sample in the middle (the “ligament”) of the sample. Fig. 6a and Fig. 6b describes the fracture. The data set for the PU/PAA samples show minimal variation – samples 1–3 represent a repeatable data set. These curves are shown in Fig. 7.

The data set for the pure PU samples also shows minimal variation, the two samples tested agree with each other. These curves are shown in Fig. 8a. The PU/PAA samples have a maximum stress of 16 MPa and a maximum normalized displacement of 1.45. The PU/PAA samples also have an overall energy density of 80.9 N/mm. This energy density is obtained by normalizing the total energy expended by the ligament cross-sectional area. It is noted that the overall energy density includes

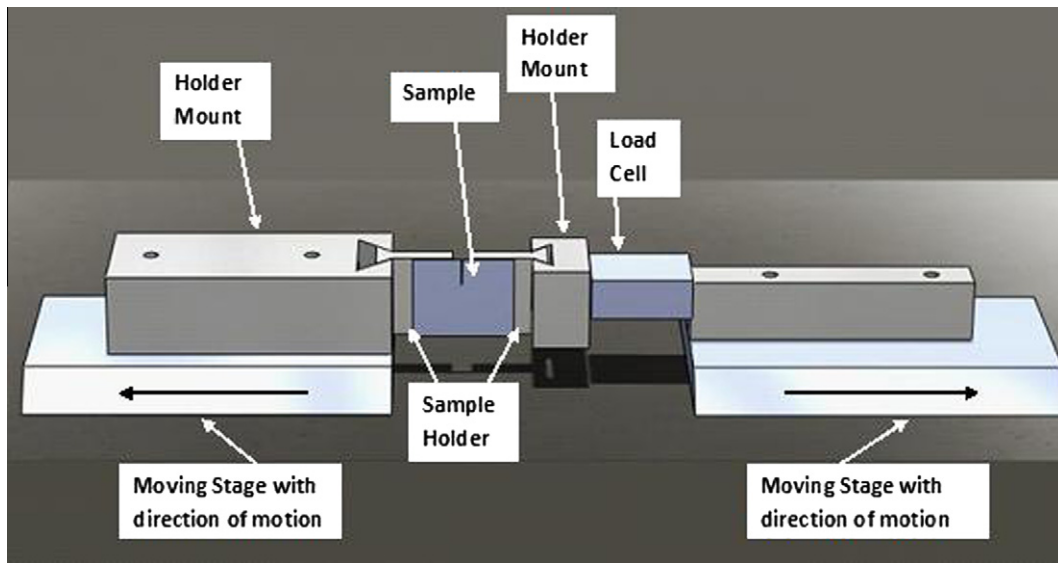


Fig. 5. Experimental setup.

the energy expended in the plastic deformation of the substrate as well as the fracture of the specimen. The PU fracture tests show that the pure polyurethane has a much lower maximum stress of 4 MPa, but a higher normalized displacement of 4.16. The overall energy density of pure PU is 58.2 N/mm. Fig. 8b is a comparison of the normalized force against normalized displacement curves for pure PU and PU/PAA.

### 2.5. Crack location of fracture tests

The speckle patterns on either side of the crack tip are analyzed by following the deformation history of selected isolated speckles on either side of the crackpath. For each unique pair of speckles, the relative change of distance–horizontal displacement plots are obtained as in Fig. 9. It is determined that the crack has moved between a pair of speckles when the rate of relative change of distance between them increases abruptly, indicating that the material between them has broken at that time step. In this manner, the instantaneous crack position as a function of time, and hence, as a function of external load is recorded. A typical crack position graph for the PU/PAA sample is shown in Fig. 10.

### 2.6. Strain map of fracture tests

In addition to the force–displacement data, the speckle images are analyzed to gather other local information. The stretches in the 1 direction are analyzed at specific points in the specimen as the crack grows. Partial unloading is observed as the crack moves past specific points. Plots for the PU/PAA samples are included in Figs. 11 and 12.

The Lagrangian strain tensor  $E_{ij}$  can be related to several deformation measures as shown in [12]. The  $E_{11}$  component strain is related to the principal stretch  $\lambda_1$  through:

$$\lambda_1 = \sqrt{1 + 2E_{11}} \quad (1)$$

where

$$E_{11} = \frac{du_1}{dX_1} + \frac{1}{2} \left[ \left( \frac{du_1}{dX_1} \right)^2 + \left( \frac{du_2}{dX_1} \right)^2 \right] \quad (2)$$

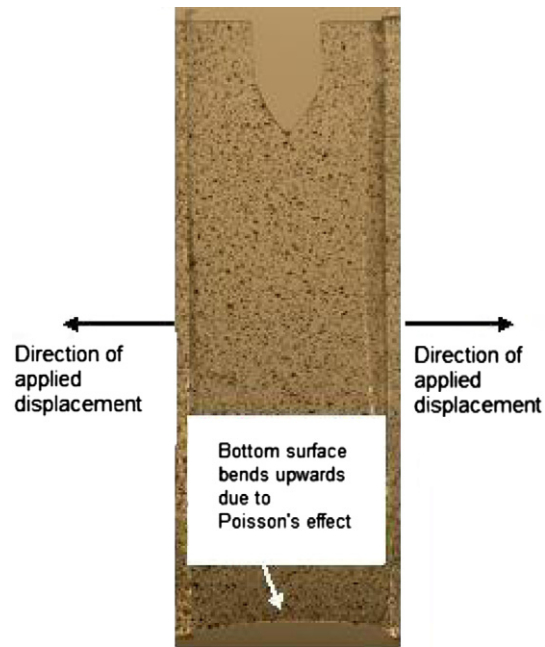
and,

$$u_i = x_i - X_i \quad (3)$$

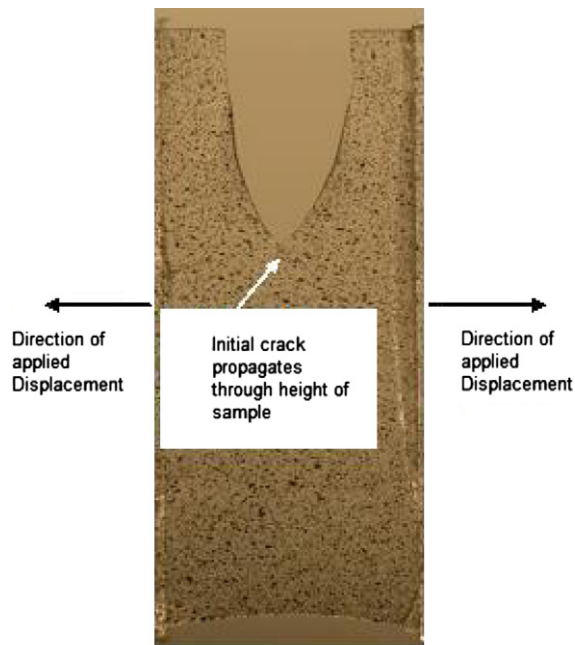
Here,  $u_i$  is the  $i$ th displacement component which is related to the undeformed,  $X_i$ , and deformed,  $x_i$ , coordinates of the material point being analyzed.

### 2.7. Full-field strain maps and fracture stress calibration

In addition to the stretches computed as described above, Aramis software version 1.6 is used to calculate strain maps of the sample during deformation. A sample strain,  $E_{11}$ , map is shown in Fig. 13. The Aramis strain maps show that a strain



(a) Experimental photograph of Fracture at timestep  $t$



(b) Experimental photograph of Fracture at timestep  $t + \delta t$

**Fig. 6.** Description of fracture. Initial crack propagates through the height of the sample, resulting in fast fracture.

concentration moves ahead of the crack tip. The onset of the strain concentration signals the activation of the fracture event. Consider a horizontal line drawn across the Aramis plot in Fig. 13a. It is seen that the  $E_{11}$  strain is uniform across this horizontal cross section. The same horizontal line is drawn in Fig. 13b and here it is noted that the  $E_{11}$  strain is no longer uniform. This indicates that the strain at the centerline is higher than near the grips. This strain concentration indicates that there is softening in this region, allowing the strain to increase much more at this location for a given state of loading. This softening is associated with the rate dependent plastic energy that is dissipated while the crack is advancing, consequently,

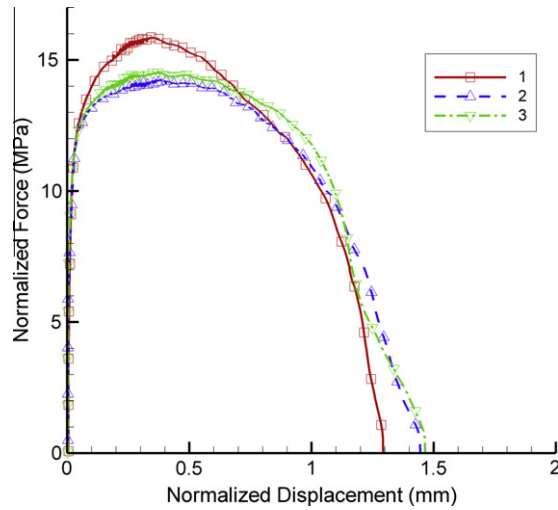


Fig. 7. Normalized fracture curves for 5 film PU/PAA stacks.

capturing this plastic dissipation accurately is needed in order to extract the fracture toughness of the films. The stress at which the fracture event is activated can be identified by examining the true stress–true strain curve from the material characterization tests. Since the full-field strains are extracted from the Aramis data, correlating this strain to the true stress–true strain curve allows determination of the local stress. This process is repeated for different points along the centerline and a fracture stress calibration is obtained in the form of an *R*-curve [9,8]. The experimental fracture stresses as a function of position as well as the *R*-curve representing the changing resistance to crack advance are shown in Fig. 14. This measured distribution of cohesive strength is important in establishing numerical models for studying fracture of these films.

### 3. Finite element model

#### 3.1. Description of the PU/PAA constitutive model

The large deformation stress–strain behavior of the polymer nanocomposite shows the following response:

1. Non-linear large strain visco-plastic behavior.
2. Strain rate dependence which is low but is present.
3. High plastic strains after unloading.

A phenomenological visco-plastic constitutive model was developed that captures the observed macroscopic mechanical response of the material. The kinematics of the constitutive model developed for the PU/PAA polymer nanocomposite is based on that for thermoplastic polyurethane (TPU), developed by Qi and Boyce [13,14], a schematic representation of which is shown in Fig. 15. There are two branches that are in parallel – a non-linear spring branch which is based on the eight-chain Arruda–Boyce model [15], and the elasto-visco-plastic component, which in turn consists of a linear elastic spring and a visco-plastic dashpot. The macroscopic deformation gradient **F** acting on both these branches is the same and the total Cauchy stress **T** is the sum of the contributions from each branch.

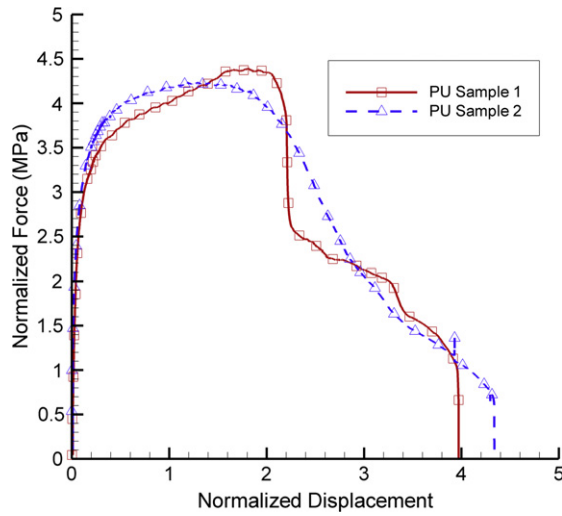
$$\mathbf{F}^N = \mathbf{F}^V = \mathbf{F} \tag{4}$$

$$\mathbf{T} = \mathbf{T}^V + \mathbf{T}^N \tag{5}$$

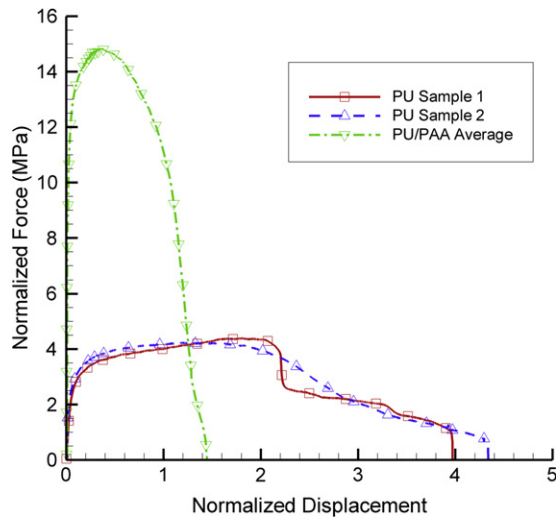
where the superscript *N* refers to the non-linear hyperelastic spring and *V* to the visco-plastic branch in the model.

The hyperelastic rubbery spring captures the entropy change due to the orientation and stretching of the molecular network. The eight-chain model developed by Arruda and Boyce [15], is used in computing the stresses as it captures the equilibrium large stretch behavior accurately. Volume changes are neglected in this branch by computing the stresses based on the deviatoric part of the macroscopic deformation gradient as shown below. The reader is referred to [15] for more details of the present model. The expression for the Cauchy stress in this branch has the form:

$$\mathbf{T}^N = \frac{\mu_r}{3J} \frac{\sqrt{N}}{\lambda_{chain}} L^{-1} \left( \frac{\lambda_{chain}}{\sqrt{N}} \right) \bar{\mathbf{B}} \tag{6}$$



(a) Normalized fracture curve for pure polyurethane



(b) Normalized fracture curve for pure polyurethane and 5 film PU/PAA Stack

Fig. 8. Normalized fracture curves for (a) pure polyurethane and (b) PU/PAA and pure polyurethane.

$$\lambda_{chain} = \sqrt{\frac{\bar{\lambda}_1^2 + \bar{\lambda}_2^2 + \bar{\lambda}_3^2}{3}} \tag{7}$$

$$\bar{\mathbf{F}}^N = J^{-1/3} \mathbf{F}^N \tag{8}$$

$$\bar{\mathbf{B}} = \bar{\mathbf{F}}^N \bar{\mathbf{F}}^{N^T} \tag{9}$$

$$\bar{\mathbf{B}}' = \bar{\mathbf{B}} - \frac{1}{3} tr(\bar{\mathbf{B}}) \mathbf{I} \tag{10}$$

$$L^{-1}(\xi) \approx \xi \frac{3 - \xi^2}{1 - \xi^2} \tag{11}$$

where  $\mu_r = nk\Theta$ , with  $n$  being the chain density (number of molecular chains per unit reference volume) of the underlying macromolecular network,  $k$  is the Boltzmann's constant and  $\Theta$  is the absolute temperature.  $N$  is the number of "rigid links" between two crosslinks and  $\mathbf{B}$  is the isochoric left Cauchy–Green tensor.  $\lambda_{chain}$  is the stretch on each chain in the eight-chain

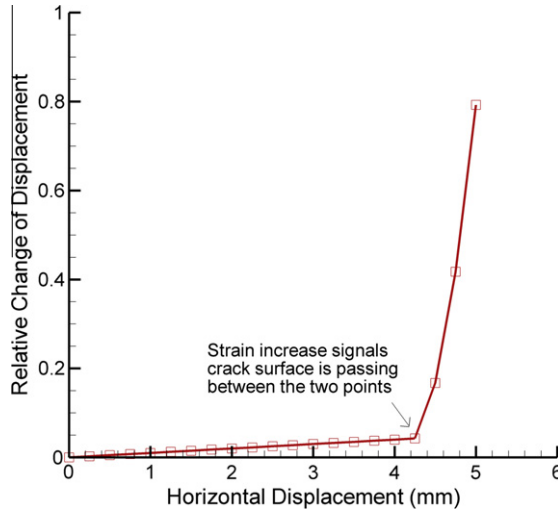


Fig. 9. Sample strain of two dots on either side of crack surface.

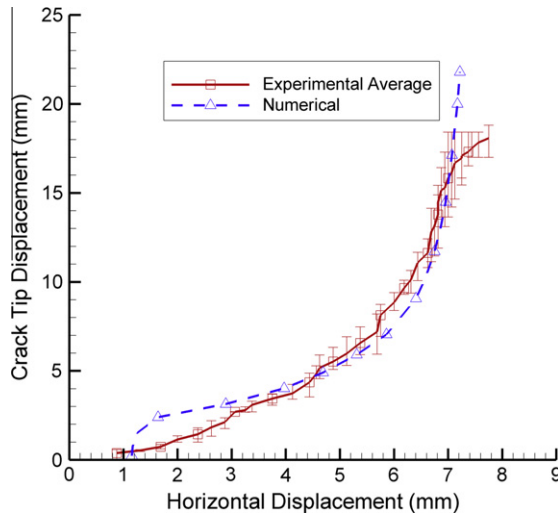


Fig. 10. Comparison of experimental and numerical crack position curves for 5 film PU/PAA stack.

network that is computed based on the squares of the principal stretches  $\lambda_1, \lambda_2$  and  $\lambda_3$ , which are obtained by the spectral decomposition of the left Cauchy–Green strain tensor.

The elasto-visco-plastic branch has a multiplicative split of the deformation gradient, which is used in computing the part of the deformation seen by the linear elastic spring. The initial elastic part of the overall non-linear macroscopic response of the material is accounted for through the stress contribution from the linear spring.

$$\mathbf{F}^V = \mathbf{F}^{Ve} \mathbf{F}^{Vb} \tag{12}$$

where  $\mathbf{F}^{Ve}$  is the deformation gradient of the elastic spring and  $\mathbf{F}^{Vb}$  is the deformation gradient of the visco-plastic dashpot. Furthermore, the decomposition of the velocity gradient  $L_V$  gives

$$\mathbf{L}^V = \dot{\mathbf{F}}^V \mathbf{F}^{V-1} = \dot{\mathbf{F}}^{Ve} \mathbf{F}^{Ve-1} + \mathbf{F}^{Ve} \dot{\mathbf{F}}^{Vb} \mathbf{F}^{Vb-1} \mathbf{F}^{Ve-1} \tag{13}$$

$$\mathbf{L}^{Vb} = \dot{\mathbf{F}}^{Vb} \mathbf{F}^{Vb-1} = \mathbf{D}^{Vb} + \mathbf{W}^{Vb} \tag{14}$$

where  $\mathbf{D}^{Vb}$  and  $\mathbf{W}^{Vb}$  are the rate of stretching and the spin, respectively.

Without loss of generality, we take [16]

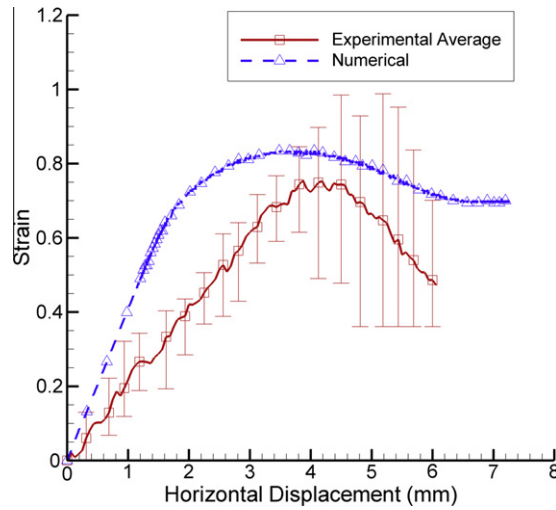


Fig. 11. Comparison of experimental and numerical strain curve at  $Y = 5$  mm for 5 film PU/PAA stack.

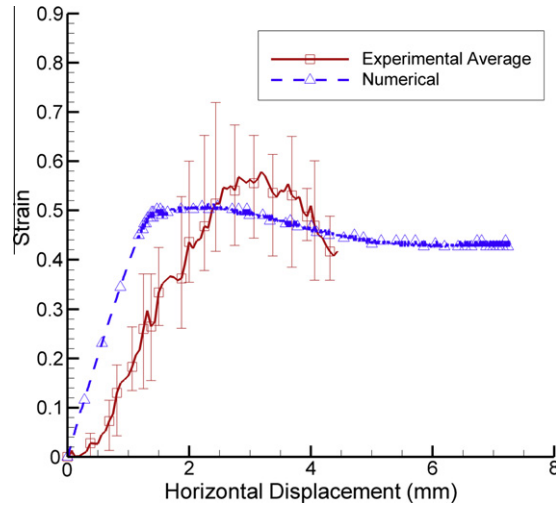


Fig. 12. Comparison of experimental and numerical strain curve at  $Y = 7.5$  mm for 5 film PU/PAA stack.

$$\mathbf{F}^{Ve} = \mathbf{V}^{Ve} \mathbf{R}^{Ve} \quad (15)$$

$$\mathbf{T}^V = \frac{1}{\det \mathbf{F}^{Ve}} \mathbf{L}^e (\ln \mathbf{V}^{Ve}) \quad (16)$$

$$\mathbf{W}^{Vv} = 0 \quad (17)$$

where,  $\mathbf{L}^e$  is the fourth-order tensor modulus of elastic constants;  $\mathbf{V}^{Ve}$  and  $\mathbf{R}^{Ve}$  are the left stretch tensor and the rotation tensor, obtained from the polar decomposition of the elastic deformation gradient.

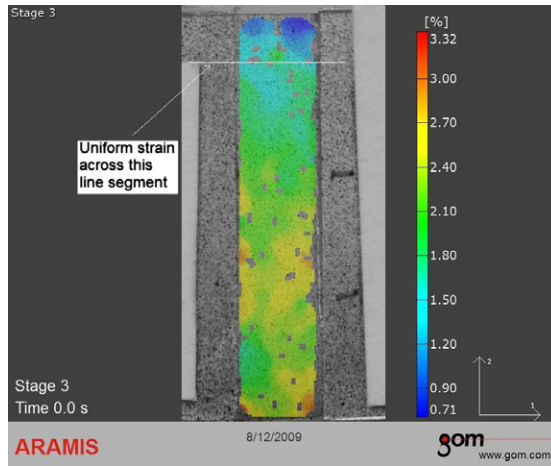
The visco-plastic stretch rate  $\mathbf{D}^{Vv}$  is constitutively prescribed as

$$\mathbf{D}^{Vv} = \frac{\dot{\gamma}^v}{\sqrt{2}\tau_v} \bar{\mathbf{T}}^v \quad (18)$$

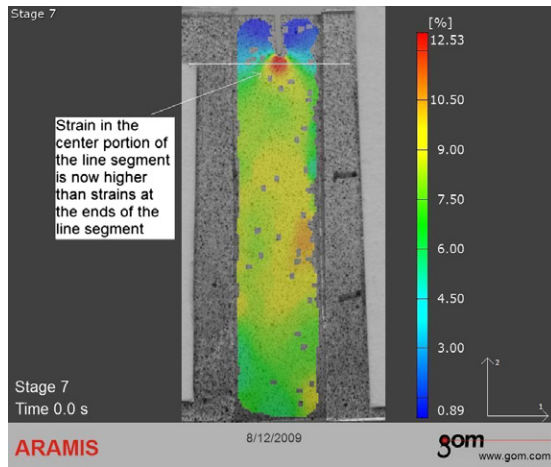
where  $\dot{\gamma}^v$  denotes the visco-plastic shear strain rate and  $\tau_v$  is the equivalent shear stress. The constitutive equation for the evolution of visco-plastic shear strain rate is given as

$$\dot{\gamma}^v = \dot{\gamma}_0 \exp \left[ -\frac{A \cdot s}{k\Theta} \left[ 1 - \left( \frac{\tau_v}{s} \right) \right] \right] \quad (19)$$

in which  $\dot{\gamma}_0$  is the pre-exponential factor proportional to the attempt frequency and  $s$  is the athermal shear strength, which represents the resistance to the visco-plastic shear deformation.



(a) Strain map at timestep 90s (0.0584mm, 41.21N)



(b) Strain map at timestep 210s (0.3756mm, 68.16N)

Fig. 13. Aramis strain maps.

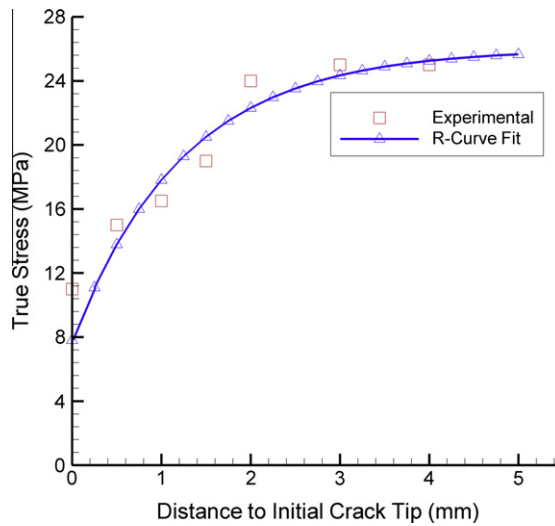


Fig. 14. Stress calibration for PU/PAA.

$$\overline{\tau}_v = \left[ \frac{1}{2} \overline{\mathbf{T}}^{v'} : \overline{\mathbf{T}}^{v'} \right] \tag{20}$$

The rate and temperature dependency of the material is captured within the evolution equations for the dashpot.

The uniaxial tension tests performed on PU/PAA polymer nanocomposite helps in understanding the overall macroscopic response of the material during loading and unloading. In the use of the constitutive model for the numerical computation of fracture toughness, it is essential to fit both the loading and unloading, so as to accurately match the area under the stress–strain curve. On comparing the mechanical behavior of polyurethane with that of PU/PAA nanocomposite, we notice significantly higher residual plastic strains after unloading in the latter. The evolution in the athermal shear strength is essential in fitting the unloading response of the polymer nanocomposite [17]

$$\dot{s} = h(1 - s/s_{ss})\dot{\gamma}^p \quad \text{with, } s(0) = s_0, s(\infty) = s_{ss} \tag{21}$$

where  $h$  is a measure of the rate of increase in  $s$ .

### 3.2. Implementation of the constitutive model and identification of material parameters

A fully three-dimensional model based on the described constitutive equations was implemented as a user defined material (umat) subroutine in the commercial finite element application Abaqus. This subroutine was used in running simulations at the same strain rates as used in the experimental uniaxial tensile tests. The material parameters were varied to fit the true stress vs. true strains for the polymer nanocomposite. All simulations were run at a constant temperature of 296 K with pre-scribed displacement vs. time function.

Comparison of the results from the uniaxial tension experiments and the simulations show the following key characteristics of the constitutive model. These are compared in Figs. 16–18 for slow through fast rates of strain.

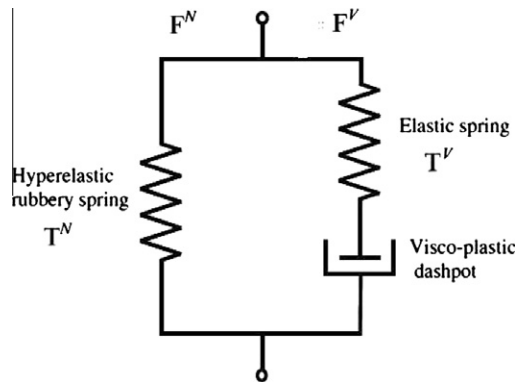


Fig. 15. Constitutive model.

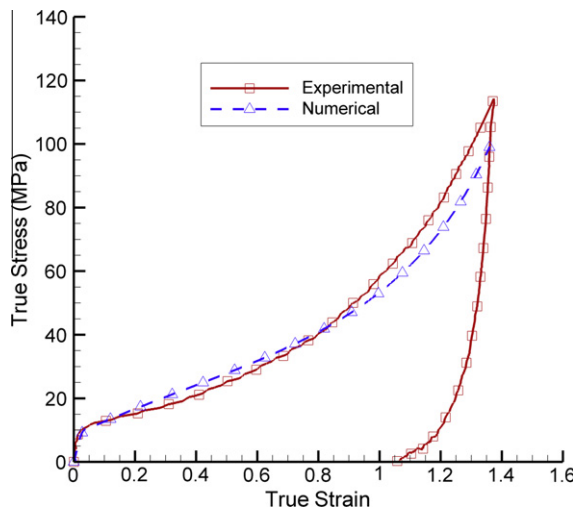


Fig. 16. Experimental and numerical substrate model comparison of PU/PAA at 0.005/s.

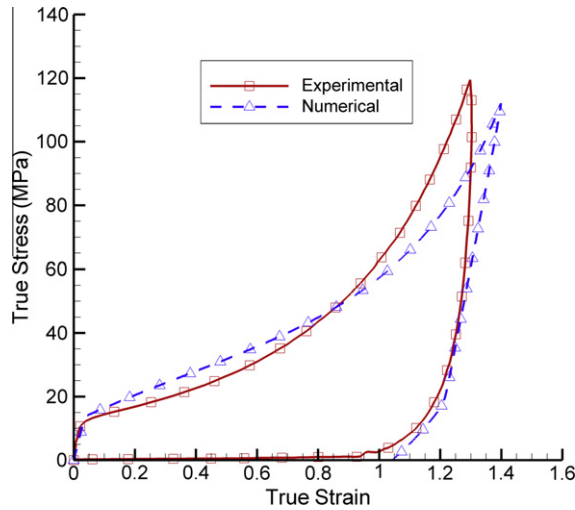


Fig. 17. Experimental and numerical substrate model comparison of PU/PAA at 0.05/s.

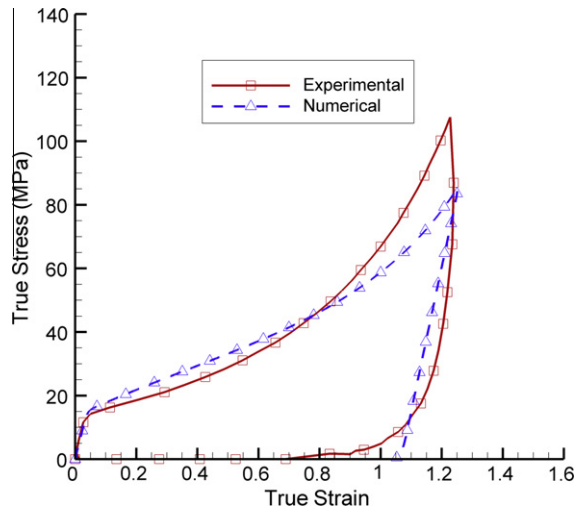


Fig. 18. Experimental and numerical substrate model comparison of PU/PAA at 0.1/s.

- The general non-linear response of the material during loading is matched well as we observe the initial elastic response followed by the strain hardening and finally the steep rise in the stresses.
- The low strain rate dependency is incorporated by adjusting the parameters associated with the visco-plastic dashpot.
- The shape of the unloading curve and the residual plastic strains can be satisfactorily matched with the experimental results. This allows for a good comparison of the area under the loading–unloading curve in both the experiments and simulation.

The determination of material parameters was done based on the experimental data. The value of Young’s modulus  $E$  was found by measuring the initial slope of the stress–strain curve. Poisson’s ratio  $\nu$  was taken to be 0.30. The initial athermal shear yield strength  $s_0$  is calculated from the elastic constants (refer to Table 1). The strain rate and temperature dependence of the initial yield are modeled with the material constants  $\dot{\gamma}_0$  and  $A$ . To obtain these constants, (19) is rearranged to be an equation for a line

$$\ln(\dot{\gamma}^v) = B + C \left( \frac{\bar{\tau}_v}{S} \right) \tag{22}$$

$$C = \frac{A \cdot S}{k\theta} \tag{23}$$

$$B = \ln(\dot{\gamma}_0) - C \tag{24}$$

**Table 1**  
Material parameters for PU/PAA.

Material property	Symbol	Value
Young's modulus	$E$	620 [MPa]
Poisson's ratio	$\nu$	0.30
Pre-exponential factor	$\dot{\gamma}_0$	$10^5$ [ $s^{-1}$ ]
Rate of resistance drop w.r.t. plastic strain	$A$	$3.5 \times 10^{-18}$ [ $mm^3$ ]
	$h$	60 [MPa]
Locking stretch	$C_r = nk\Theta$	9.5 [MPa]
	$\sqrt{N}$	$\sqrt{1.80}$
Initial athermal shear yield strength	$s_0$	$0.77 \frac{\mu}{1-\mu}$
Steady state value of athermal yield strength	$s_{ss}$	$1.80 \cdot s_0$

The tensile locking stretch  $\sqrt{N}$  can be estimated by computing the limiting strain found from the stress–strain curves  $e^{e_i}$ . An initial approximation for  $\mu_r$  can be determined by measuring the initial slope of the strain hardening curve in the experimental data. The parameters,  $h$  and  $s_{ss}$ , are found by trial and error method, to find the best fit for both the loading and unloading part of the curve.

The material parameters identified for the PU/PAA nanocomposite are given in Table 1.

### 3.3. Description of the polyurethane material model

Modeling of the mechanical response of polyurethane is done based on the same phenomenological approach taken for the PU/PAA polymer nanocomposite. As a first attempt to model the polyurethane films, the constitutive model for thermoplastic polyurethanes by Qi and Boyce [14] was used. This model presents a limitation in accurately simulating both the loading and unloading part of the uniaxial tests. Hence, the constitutive model for the polymer nanocomposite is applied and the material parameters identified based on the experimental results from polyurethane films. The comparison of the material behavior of polyurethane with respect to the PU/PAA clearly shows a comparatively lower initial elastic stiffness and lower yield stress, which are reflected in the material parameters identified for polyurethane. The material parameters for PU and PU/PAA capture the unloading part of the response after matching the loading part of the response consistently.

Comparison of the results from the uniaxial tension experiments and the simulations show the following key characteristics of the constitutive model. These are compared in Figs. 19 and 20 for slow through fast rates of strain.

The material properties for PU are given in Table 2.

### 3.4. Description of the DCZM model

The DCZM model is comprised of eight-node user elements, with four nodes residing on either fracture surface. These nodes generate binding forces with their corresponding pair on the opposite fracture surface, while the fracture energy and binding forces are computed using the current surface area calculated from the positions of the four nodes. The interpretation of the fracture toughness is with respect to the *current area* of the fracture surface, since the thickness of the frac-

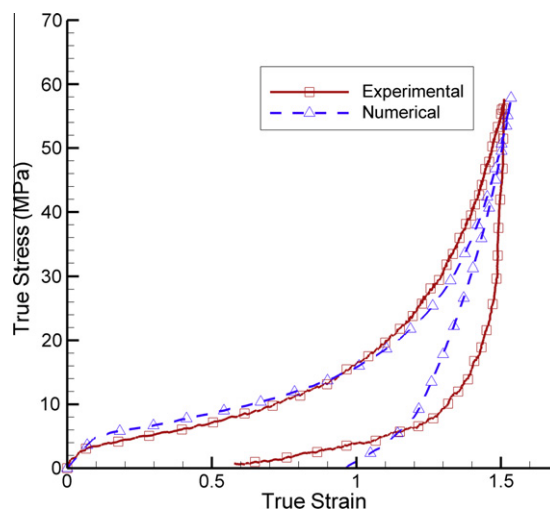


**Fig. 19.** Experimental and numerical substrate model comparison of polyurethane at 0.005/s.

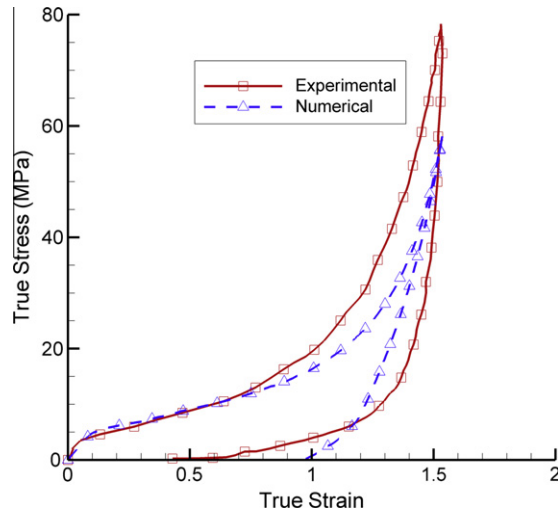


Fig. 20. Experimental and numerical substrate model comparison of polyurethane at 0.1/s.

Table 2  
Material parameters for pure PU.

Material property	Symbol	Value
Young's modulus	$E$	50 [MPa]
Poisson's ratio	$\nu$	0.45
Pre-exponential factor	$\dot{\gamma}_0$	0.1 [ $s^{-1}$ ]
	$A$	$2.0 \times 10^{-17}$ [ $mm^3$ ]
Rate of resistance drop w.r.t. plastic strain	$h$	5.5 [MPa]
	$C_r = nk\theta$	1 [MPa]
Locking stretch	$\sqrt{N}$	$\sqrt{9.60}$
Initial athermal shear yield strength	$s_0$	$0.77 \frac{\mu}{1-\mu}$
Steady state value of athermal yield strength	$s_{ss}$	$2.0 \cdot s_0$

ture specimen is not constrained to remain constant. Other details of the DCZM model, which includes finite rotations, are described in [11].

A modified trapezoidal traction-separation law is used for the elements. The modified traction-separation law is based upon the trapezoidal traction-separation law for ductile materials [18], as shown in Fig. 21. The traction-separation law is

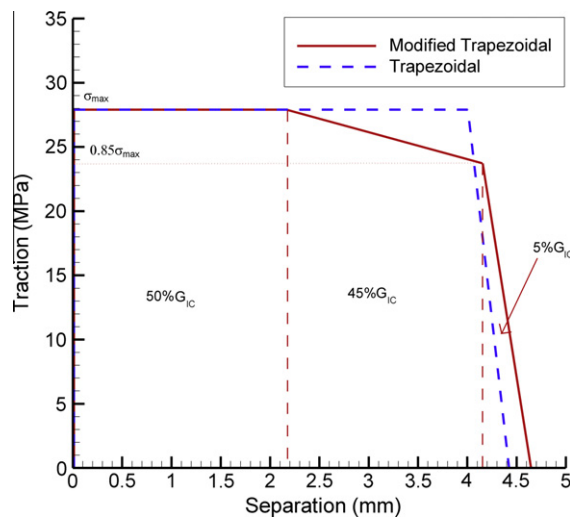


Fig. 21. Traction separation laws used in the simulations.

modified by adding an additional shallower relaxation stage. This additional relaxation stage was deemed necessary for the numerical model to converge while allowing for large deformations in the fracture process. The modified traction separation law is shown in Fig. 21, with the proportion of the fracture toughness allocated to each stage as indicated in the figure, as well as the stress turning points. Note that the fracture toughnesses of both traction-separation laws shown are the same. An  $R$ -curve [9] is applied to the fracture toughness used by each element as follows:

$$G_{1c}(\delta) = G_{1c}^{SS} * \left(1 - \omega * e^{-\frac{\delta}{\gamma}}\right) \quad (25)$$

where  $\delta$  is the distance of the element to the initial fracture surface,  $\omega$  is the  $R$ -curve growth proportion and  $\gamma$  is the  $R$ -curve decay rate. An example of the shape of a  $R$ -curve is included in Fig. 22. From the fracture stress calibration that was discussed earlier, a  $R$ -curve for the fracture strength is obtained as,

$$\sigma_{max}(\delta) = \sigma_{max}^{SS} * \left(1 - \omega * e^{-\frac{\delta}{\gamma}}\right) \quad (26)$$

Each DCZM element has the prescribed properties shown in Table 3.

### 3.5. Description of the numerical model

The numerical model for the PU/PAA experiment is composed of 12,060 nodes organized in 4160 eight node plane-stress elements. The specimen is modeled using optically captured dimensions of the film. The left and right boundaries are fixed in the 2 and 3 directions. The right boundary is displaced only in the 1 direction at a rate of 7.5 mm over 2500 s to match the experimental displacement rate. The 3 dimensional numerical model is included in Fig. 23. The process is repeated for the PU/PAA experiment. During the solution process, the reaction force and displacement of the right boundary is output to a text file. In addition, the numerical solver also gives out the nodal displacements of selected substrate and DCZM elements in order to calculate the relevant mechanical parameters to interpret the results.

### 3.6. Results of the numerical model predictions for for PU/PAA and pure polyurethane

Iterating the DCZM elements for different  $R$ -curve variations and fracture toughnesses, a full match for the force–displacement curve is obtained and is shown in Fig. 24. The match is obtained at a critical fracture toughness of 65.4 N/mm. In addition,

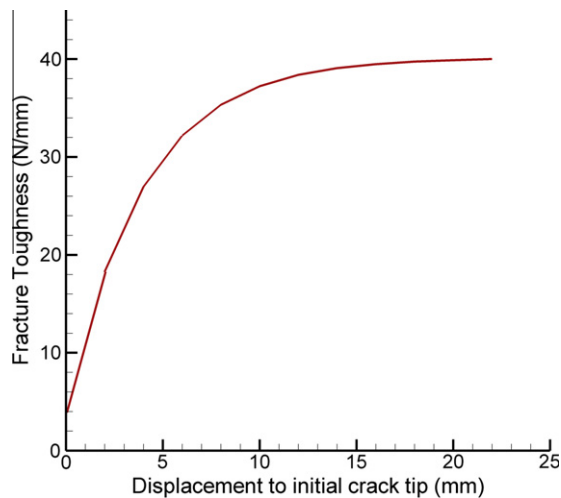
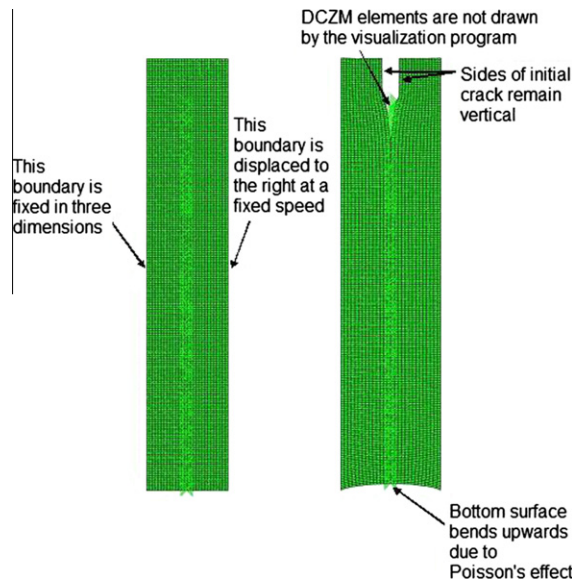


Fig. 22. Fracture toughness with respect to displacement.

**Table 3**  
DCZM properties.

Maximum steady state stress	$\sigma_{max}^{SS}$
Stead state fracture toughness	$G_{1c}^{SS}$
$R$ -curve growth proportion	$\omega$
$R$ -curve decay rate	$\gamma$
Various shape factors	$G_{1c}^i, \sigma_{max}^i, i = 1, \dots, 4$



**Fig. 23.** 3D Abaqus model of the fracture sample. The left and right boundaries are under full displacement control in three dimensions, the film is allowed to deform in the thickness direction. The DCZM elements are denoted by the crosses ( $\times$ ) in the right hand view.

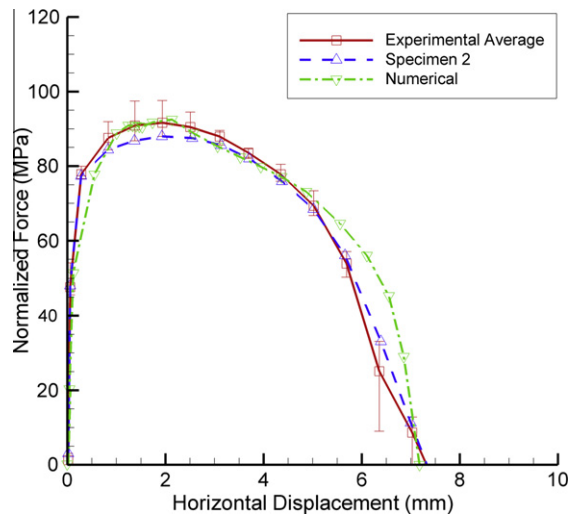


**Fig. 24.** Comparison of experimental and numerical force–displacement curves for 5 film PU/PAA stack.

tion to the force–displacement curve, the crack point location of the experiment is also accurately matched. The crack point location is obtained in a similar fashion as in the experiment. The comparison is included in Fig. 10. The numerical prediction also show a close match for the initial slope of the strain–time plots at two locations on the substrate in Figs. 11 and 12. The initial slope of the numerical strain closely matches the experimental slope. The turning point of the numerical strain matches the turning point of the experiment.

In a similar manner, a full match for the force–displacement curve for pure polyurethane is obtained and shown in Fig. 25. The match is obtained at a critical fracture toughness of 61 N/mm. It is noted that fracture toughness of pure polyurethane obtained in this manner maybe slightly overpredicted because the constitutive model that is used in the finite element predictions stores less plastic energy than required.

### 3.7. SEM In situ experiments

Usually, the addition of nano-particles to a polymer material leads to a decrease in ductility and a corresponding decrease in fracture toughness. In the results reported here, the fracture toughness of stiffened polyurethane has been shown to be

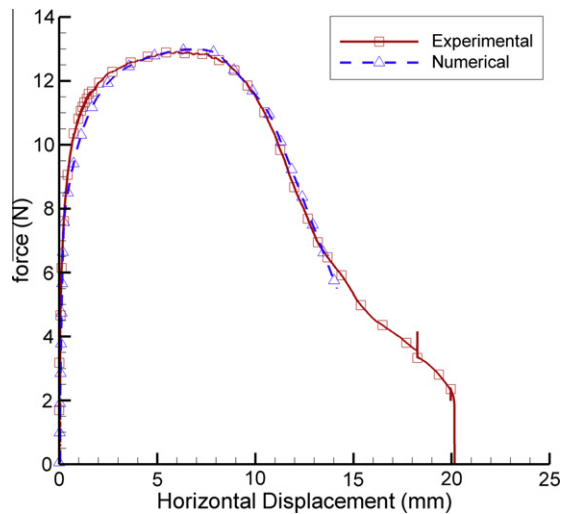


Fig. 25. Comparison of experimental and numerical force–displacement curves for pure polyurethane.

slightly larger than the non-stiffened polyurethane. Thus, it is worthy to examine the mechanisms responsible for elevating the fracture toughness. In order to do this, single-edge-notch tension fracture tests are carried out *in situ* in a scanning electron microscope. These tests allow observation of the micron-scale and high nano-scale fracture mechanisms present in the composite and unstiffened polymer.

It is observed that the layering of the nanocomposite results in large amounts of inter-layer shearing, similar to the delamination toughening reported in layered systems like Aluminum–Lithium as reported in [19]. The inter-layer shearing results in the expenditure of a larger amount of energy during the fracture process. Additional energy is expended when micron sized voids grow when engulfed by the elevated stress process zone around the advancing crack. These new results will be presented elsewhere.

#### 4. Concluding remarks

The fracture toughness of exponential LBL manufactured PU/PAA films has been measured through a combination of experiment and finite element based simulation. Due to the large deformations associated with the fracture event, an accurate constitutive model, validated through experiments, has been used in conjunction with a new finite deformation based formulation of the discrete cohesive zone model to extract the fracture toughness. Experimental results for full-field time histories of the strain maps in the fracturing film have been analyzed to obtain the *R*-curve parameters for the five stack film. This *R*-curve behavior implies the presence of toughening mechanisms at work in the fracture process zone. The experimental and numerical results presented in the paper show good agreement for the PU/PAA films as well as for similar fracture tests with pure polyurethane films. For the PU/PAA films, the mode-I fracture toughness was found to be 65 N/mm, while for the pure PU this value was 61 N/mm. It should be noted that stiffened composites generally have lower fracture toughnesses with respect to their unstiffened base materials. In view of the enhanced stiffness and strength of the PU/PAA [5], the LBL manufacturing process has resulted in a material with elevated stiffness and strength, while also elevating the fracture toughness.

#### References

- [1] Coyne KJ, Qin XX, Waite JH. Extensible collagen in mussel byssus: a natural block copolymer. *Science* 1997;277(5333):1830–2.
- [2] Barthelat F, Espinosa HD. An experimental investigation of deformation and fracture of nacre-mother of pearl. *Exp Mech* 2007;47(3):311–24.
- [3] Chen Q, Chasiotis I, Chen C, Roy A. Nanoscale and effective mechanical behavior and fracture of silica nanocomposites. *Compos Sci Technol* 2008;68(15–16):3137–44.
- [4] Decher G. Fuzzy nanoassemblies: toward layered polymeric multicomposites. *Science* 1997;277(5330):1232–7.
- [5] Podsiadlo P, Arruda EM, Kheng E, et al. LBL assembled laminates with hierarchical organization from nano- to microscale: high-toughness nanomaterials and deformation imaging. *ACS Nano* 2009;3(6):1564–72.
- [6] Podsiadlo P, Kaushik AK, Arruda EM, Waas AM, Shim BS, Xu JD, et al. Ultrastrong and stiff layered polymer nanocomposites. *Science* 2007;318(5847):80–3.
- [7] Podsiadlo P, Michel M, Lee J, Verploegen E, Kam NWS, Ball V, et al. Exponential growth of LBL films with incorporated inorganic sheets. *Nano Lett* 2008;8(6):1762–70.
- [8] Suo Z, Fan B. Delamination *R*-curve phenomena due to damage. *J Mech Phys Solids* 1992;40(1):1–16.
- [9] Gdoutos EE. Crack growth based on energy balance. *Fracture mechanics criteria and applications*. Norwell (MA): Kluwer Academic Publishers; 1990. p. 112–59 [Chapter 4].
- [10] Xie D, Waas AM. Discrete cohesive zone model for mixed-mode fracture using finite element analysis. *Engng Fract Mech* 2006;73(13):1783–96.

- [11] Xie D, Salvi AG, Sun C, et al. Discrete cohesive zone model to simulate static fracture in 2D triaxially braided carbon fiber composites. *J Compos Mater* 2006;40(22):2025–46.
- [12] Fung YC. *A first course in continuum mechanics*. Englewood Cliffs (NJ): Prentice-Hall; 1969.
- [13] Qi HJ, Boyce MC. Constitutive model for stretch-induced softening of the stress-stretch behavior of elastomeric materials. *J Mech Phys Solids* 2004;52:2187–205.
- [14] Qi HJ, Boyce MC. Stress–strain behavior of thermoplastic polyurethane. *Mech Mater* 2005;31:817–39.
- [15] Arruda EM, Boyce MC. A three-dimensional constitutive model for the large stretch behavior of rubber elastic materials. *J Mech Phys Solids* 1993;41:389–412.
- [16] Boyce MC, Weber GG, Parks DM. On the kinematics of finite strain plasticity. *J Mech Phys Solids* 1989;37:647–65.
- [17] Boyce MC, Parks DM, Argon AS. Large inelastic deformation of glassy polymers, part I: rate-dependent constitutive model. *Mech Mater* 1988;7:15–33.
- [18] Sun C, Thouless MD, Waas AM, Schroeder JA, Zavattieri PD. Ductile–brittle transitions in the fracture of plastically deforming, adhesively bonded structures. Part II: numerical studies. *Int J Solids Struct* 2008;45:4725–38.
- [19] Rao KTV, Ritchie RO. Mechanisms influencing the cryogenic fracture-toughness behavior of aluminum–lithium alloys. *Acta Metall Mater* 1990;38(11):2309–25.